Plasma Chem Plasma Process (2018) 38:461–484
https://doi.org/10.1007/s11090-018-9889-z

ORIGINAL PAPER

The Production of Ketene and C_5O_2 from CO_2, N_2 and CH_4 in a Non-thermal Plasma Catalysed by Earth-Abundant Elements: An In-Situ FTIR Study

P. A. Christensen[1] · Abd Halim Bin Md Ali[1] · Z. T. A. W. Mashhadani[1] · M. A. Carroll[2] · P. A. Martin[3]

Received: 21 January 2018 / Accepted: 17 March 2018 / Published online: 23 March 2018

Abstract In situ Fourier Transform Infra Red spectroscopy was employed to study the plasma glow region of a non-thermal plasma between two Macor dielectrics and fed with CO_2, CH_4 and N_2. CO, HCN and formaldehyde were produced and rapidly attained steady-state conditions. In addition, the chain oxides C_5O_2 and ketene were observed (the first time such species have been seen in the dry reforming of methane) and a liquid film was produced comprising multiple components, one of which was acetamide. The data were interpreted in terms of catalysis by the Macor dielectric and a wholly novel, multizone model in which the liquid film plays a direct and important role. The data obtained in the plasma experiments were compared to an analogous, thermal experiment. Importantly, the results from this work could have major implications across the fields of catalysis, synthesis and origin-of-life chemistry.

Keywords Non-thermal plasma · Ketene · CO_2 · Conversion · Catalysis · Infrared spectroscopy · Acetamide · C_5O_2

Electronic supplementary material The online version of this article (https://doi.org/10.1007/s11090-018-9889-z) contains supplementary material, which is available to authorized users.

✉ P. A. Christensen
paul.christensen@ncl.ac.uk

[1] School of Engineering, Newcastle University, Bedson Building, Newcastle upon Tyne NE1 7RU, UK

[2] School of Natural and Environmental Sciences, Newcastle University, Bedson Building, Newcastle upon Tyne NE1 7RU, UK

[3] School of Chemical Engineering and Analytical Science, The University of Manchester, Oxford Road, Manchester M13 9PL, UK

Introduction

Non-thermal plasma at atmospheric pressure is produced by the partial ionization of a gas by electron impact using high AC or pulsed high voltages in the kV range. The temperature of the electrons in such plasmas is typically 10^4–10^5 K, whilst the heavier species such as the ions and gas molecules remain at temperatures close to ambient. This generates radicals, ions and vibrationally and electronically excited species not normally present in thermal equilibrium at room temperature [1, 2].

To date, it is generally perceived that plasma-driven catalytic (plasma catalytic) syntheses are too expensive in energy terms to compete with standard, thermal processes. However, one highly topical potential application where energy efficiency is not a primary driver is the use of electricity from renewable sources to generate chemical products. Matching the production of electricity from renewable energy to demand is very difficult, and often the surplus is simply spilled: the storage of this surplus energy chemically by plasma catalysis is seen as a possible solution to this problem. The exciting prospect that plasma-catalysis may generate different, and potentially novel products, when compared to the conventional thermal process also offers a firm foundation for the development of this pioneering technology.

Plasma catalysis has a number of potential advantages: thus, in principle, almost 97% of the discharge power of such plasmas can be converted into vibrational excitation of the gas feed molecules [3, 4]. Adding a catalyst can speed up the chemical processes in a plasma and/or offer alternative mechanistic pathways with lower activation energies: thus, reactive species are produced and interact with the catalyst at temperatures at which most thermally-driven processes would be slow. Further, vibrationally excited molecules can have markedly different sticking probabilities and different chemistries on the surface of catalysts in contact with plasma [5] and it should be possible to enhance targeted reactions and suppress others by controlling the number density of electrons and electron and gas temperatures.

As a consequence of the potential of plasma catalysis, many systems have been studied, including [6]: ozone generation [7], the conversion of CH_4 to H_2 and C2–C4 derivatives [8], toluene to phenol and cresols [9], CO_2 and H_2O to syngas and synfuels [10], the treatment of Volatile Organic Compounds (VOCs) in waste streams [11], decontamination and disinfection [12], the deep desulfurization of diesel fuels [13] and the treatment of flue gas [14]. Typically, the reactors employed are based on cylinders of alumina or quartz with one high voltage electrode wrapped around the outer surface of the cylinder and a metal rod, mounted along the axis of the cylinder, as the second electrode [15, 16]. Catalyst pellets can be placed in the reactors [15]. Of direct relevance to the work described in this paper is the plasma-driven dry reforming of CO_2 and CH_4 [17]. In general, CO_2 and CH_4 are employed without a third feed gas, and the products observed are syngas ($CO + H_2$) with small amounts of C_2H_2, C_2H_4 etc. and very small amounts of oxygenated compounds such as ketones and alcohols.

Whilst plasma driven systems find very wide (and commercially-viable) application in industries including waste gas treatment (electrostatic precipitation [18]), ozone generation (primarily for large scale water treatment [19]) and surface treatment/etching [20], these do not involve plasma/catalyst interactions, and this is where both the challenge and opportunity lies. In essence, the brake on the development of plasma catalytic technology has been the limited understanding of the chemistry taking place in plasma and the absence of knowledge and understanding of plasma/solid (i.e. dielectric and/or catalyst) interactions

(so much so that the US Government regards the interactions of plasmas with solid surfaces as one of the six critical challenges that define the plasma research frontier [21]).

The inadequate understanding of plasma chemistry probably lies in the lack of analytical studies able to provide molecular information: thus UV Vis absorption and emission spectroscopies have been employed for a number of years in the study of plasma, as may be expected given the inevitable emission of light from plasma. Such studies give useful information on excited species (see, for example, [22–26]). However, as an analogy, the field of electrochemistry underwent a paradigm shift in the 1980s with the advent of, in particular, in situ FTIR spectroscopy with its ability to provide molecular information and hence determine the identity of adsorbed and solution intermediates and products [27, 28]. It is generally recognised that emission spectroscopy and the standard analytical techniques currently employed in NTP research need to be complemented by methods able to provide molecular information such as FTIR spectroscopy [1]. Thus, the field of NTP plasma catalysis is at a similar stage of development as electrochemistry was in the mid-1980s: whilst the plasma/catalyst surface has not been investigated extensively with in situ FTIR, such studies have started to appear. There are a number of studies on the downstream analysis of the exhaust from NTPs, see for example [29], but actual studies of the plasma glow with IR spectroscopy [30] or of the catalyst surface in contact with a plasma is only a recent phenomenon. Thus, the quality of the information that can be obtained from in situ FTIR is exemplified by the work of Li et al. on the deposition of Si from hexamethyldisiloxane plasma [31], Rivallan and colleagues on the conversion of IPA at Al_2O_3 [32], Stere et al. [33] on the hydrocarbon-assisted NO_x removal from simulated diesel fuel over silver-based catalysts, Rodriguez et al. [34] on the conversion of IPA at Al_2O_3, CeO_2 and TiO_2 and Jia and Rousseau on the plasma-assisted reaction of acetone at CeO_2 [35]. These studies employed the Diffuse Reflectance approach [33, 34], transmission through the catalyst as a wafer [32, 35] or passed the IR beam through the plasma glow above the solid surface [30]. Rivallan et al. [36] employed step scan FTIR spectroscopy to study the gas phase reduction of CO_2 in a tube reactor (i.e. they did not study the catalyst/plasma interface): however, they saw no reaction products or intermediates just the loss of CO_2, although they did achieve a time resolution of ca. 400 μs.

Recently, we published in situ FTIR studies comparing the plasma- and thermally-driven reaction of CO_2 at Macor, the first such direct comparison of plasma and thermal chemistries [37]. We showed that, in both the thermal and plasma experiments, rotational excitation of the CO_2 (CO_2*) took place in the plasma glow. In the plasma system, rotationally-excited CO (CO*) was produced by the reduction of the CO_2, with conversion up to 9% and energy efficiencies of 1–2%, in line with the literature. In contrast, no reaction of CO_2 was observed in the thermal experiments.

This paper extends the initial work to the in situ FTIR investigation of the dry reforming of CO_2 and CH_4 at Macor. In situ FTIR spectra of both the plasma and of the catalyst surface during operation enable detailed analysis of the potential benefits of plasma catalysis and explores further the apparent formation of liquid product films in these processes. The paper is structured as follows: firstly the experimental plasma catalytic reactor and measurement configurations are described; secondly, the initial characterisation of the system after a short run time followed by a detailed study of the changes observed after longer run time is described. Finally the unexpected results are discussed and possible mechanisms are proposed which could pave the way for exploiting the major, untapped potential of plasma catalysis.

Experimental

The Non-thermal Plasma Cells

The transmission NTP cell [37], see Fig. S1(a), was designed and fabricated in–house and was made from a 15 cm long, cylindrical polytetrafluoroethylene (PTFE) tube with an outer diameter of 6.3 cm and an inner diameter of 2.5 cm. The high voltage electrodes were in the form of two plungers, sealing against the inner walls of the PTFE via rubber 'O' rings. One of the plungers was hollow down its axes (a 4 mm diameter hole) and the feed gas was delivered via this channel and removed via an outlet in the top of the cell. The electrodes were covered with 5 mm thick Macor caps [Goodfellow Cambridge/quartz (35–50%), magnesium oxide (15–20%), aluminium oxide (15–20%) and fluoride (1–5%)] fitted snugly over each disc electrode, one of which had a hole aligned with the central gas delivery channel. Two infrared transparent CaF_2 windows (25 mm diameter, 3 mm thick, Crystran) were glued into the PTFE cell. The distance between the windows (path length) was 5.1 cm. The windows were positioned such that their centres aligned with the centre of the gap between the electrodes. The plasma volume was 7.4 cm^3 and the residence time at a flow rate of 200 cm^3 min^{-1} was 2.2 s.

The electrodes were connected to a NeonPro lamp transformer, NP100000-30 (Hyrite, China) which provided an output up to 10 kV at a constant frequency of 24 kHz. A voltage controller (Carroll & Meynell) was used to control the input power to the HV transformers. The input power to the plasma was monitored using a N67FU Gadget 13A Power Meter (Maplin, UK); the input powers quoted below were those obtained by subtracting the input power observed with plasma to the reading obtained with the system switched on but with no plasma initiated (4 W). The temperature of the cell was monitored using a thermometer against one of the windows during runs without spectral data collection and found to be ca. 20–25 °C over the duration of the experiments detailed below: however, the observation of hot CO_2 and CH_4 (see below) suggests that the actual temperature of the gas species in the plasma was higher.

The reflectance NTP cell [37] is shown in Fig. S1(b): the IR beam passed through a 3 mm CaF_2 plate window and a 5 mm gap before being incident on the surface of a 3 cm × 3 cm × 0.5 cm Macor plate covered by a Ti mesh (50% open area) electrode at an angle of 24 degrees. The other electrode was a 2.3 cm × 2.2 cm × 0.007 cm stainless steel foil mounted on an alumina plate behind the Macor. The same power supply etc. was employed as for the transmission cell. In contrast to the transmission cell, the plasma was in contact with a titanium mesh electrode as well as Macor. The plasma volume was 2.0 cm^3 and the residence time at a flow rate of 30 cm^3 min^{-1} was 4.0 s.

The design of the transmission cell did not allow for cooling of the electrodes apart from the 200 cm^3 min^{-1} flow of the feed gas: the reflectance cell had dedicated cooling channels for nitrogen gas, as shown in Fig. 1b.

The Plasma FTIR System

An Agilent FTS7000 FTIR spectrometer with a Deuterated TriGlycine Sulfate (DTGS) detector was employed. The IR beam was passed through the plasma via the two CaF_2 windows to the detector via an Amtir-1 filter, 25 mm × 2 mm (Spectra-Tech, USA) to remove visible light.

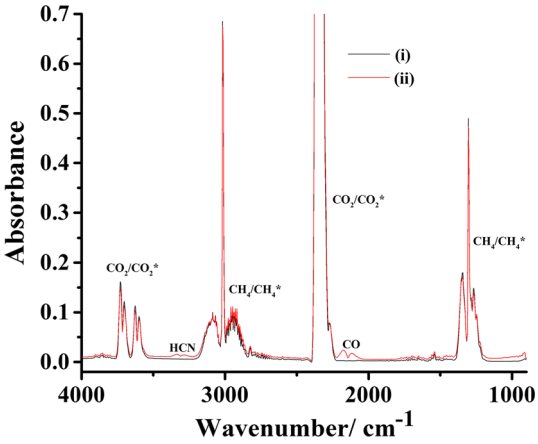

Fig. 1 In situ FTIR spectra (8 cm^{-1} resolution, 100 spectra per scan set, and 1 min per spectrum) of the 8.5% CO_2 + 13.1% CH_4 + 78.4% N_2 feed gas in the plasma transmission cell at a total flow rate of 200 cm^3 min^{-1} and a temperature of ca. 25 °C: (i) before initiating plasma and (ii) after 2 min operation at 24 W. In both cases, the reference spectrum was collected using nitrogen gas as the feed and without plasma

CO_2 (R744/100%) and CH_4 (N4.5/100%) were supplied by BOC Industrial gasses, UK. Dinitrogen was obtained from a NITROSource generator. The gasses were mixed as appropriate and the composition controlled using flow meters. The compositions of the gas feeds employed in the experiments described below are summarized in Table 1; the nominal composition intended for the gas feeds for the CO_2 + CH_4 + N_2 experiments was 10% CO_2 + 10% CH_4 + 80% N_2, with three exceptions (5% CO_2, Ar instead of N_2 and 54% CO_2). The input powers of 20 and 28 W correspond to Specific Input Energies (SIEs) of 6.0 and 8.4 kJ dm^{-3}, respectively defined as [38]:

$$\text{SIE} = \text{Discharge power (kW)}/\text{Total gas flow rate}\left(\text{dm}^3\text{s}^{-1}\right) \quad (1)$$

These correspond to average electron energies of 3.9–5.5 eV.

The cell was first flushed with N_2 at a flowrate of 200 cm^3 min^{-1} for 120 min, and a single beam spectrum taken (100 co-added and averaged scans at 8 cm^{-1} resolution, 60 s per scan set), after which the chosen feed composition was admitted to the cell at a total flow rate of 200 cm^3 min^{-1} and a second single beam spectrum collected, both without plasma. Sample spectra, S_S, were then taken as a function of time after the high voltage–power supply was switched on, and at regular intervals thereafter, up to 20 min. By using the first single beam (of the nitrogen gas with no plasma) as the reference spectrum (S_R) all of the infrared active species present in the plasma were observed; using the second single beam as the reference spectrum resulted in difference spectra, showing only the changes incurred on initiating the plasma. The flow rate employed with the reflectance cell was 30 cm^3 min^{-1} to allow sufficient residence time.

The Thermal FTIR System

In-situ FTIR experiments as a function of temperature were carried out using a Varian 670-IR spectrometer equipped with a ceramic air-cooled infrared source, a DLaTGS detector and a Specac Environmental Chamber and diffuse reflectance unit [39]. A 12.5 mm diameter, 2 mm thick Macor disc was employed as the catalyst. The Specac reflectance accessory allows IR spectra to be collected under controlled atmosphere conditions from room temperature to 600 °C and pressures from vacuum to 34 atm. The IR

Table 1 The feed gas compositions employed in the work reported in this paper, and a summary of the data obtained from the spectra collected after 2 min during the various experiments

	Composition $CO_2/CH_4/N_2$ or Ar	Power/ W	$[CO_2]_{feed}/10^{-3}$M	$[CH_4]_{feed}/10^{-3}$M	Gain CO/ 10^{-4}M	%CO	Gain HCN/ 10^{-4}M	Gain HCHO/ 10^{-4}M	Abs 2152 $cm^{-1}/10^{-3}$
1a	10.6%/13.4%/ 76.0%	20	4.3	5.5	3.7	8.6	2.5	0.04	3.2
1b	12.7%/15.9%/ 71.4%	20	5.2	6.5	6.7	12.9	3.9	?	6.3
2	8.7%/12.8%/ 78.5%	22	3.5	5.2	3.5	10.0	2.8	?	0
3a	9.7%/13.7%/ 76.6%	24	4.0	5.6	4.7	11.8	3.0	0.05	6.5
3b	8.5%/13.1%/ 78.4%	24	3.5	5.3	3.7	10.6	3.2	?	0
4	7.4%/11.0%/ 81.6%	26	3.0	4.5	4.0	13.0	3.9	?	7.1
5a	12.3%/14.4%/ 73.3%	28	5.0	5.9	6.2	12.4	3.6	?	12.2
5b	9.8%/15.7%/ 74.5%	28	4.0	6.4	5.3	13.3	5.0	?	24.0
6	15.0% CH_4 85.0% N_2	20	0	6.1	0	0	5.7	0	0
7	12.3% CH_4 87.7% N_2	22	0	5.0	0	0	4.2	0	0
8	16.2% CH_4 83.8% N_2	24	0	6.6	0	0	4.6	0	0
9	13.0% CH_4 87% N_2	26	0	5.3	0	0	6.4	0	0
10	15.0% CH_4 85.0% N_2	28	0	6.1	0	0	6.0	0	0
11	12.9% CO_2/ 87.1% N_2	20	5.3	0	5.8	10.9	0	0	0
12	9.7% CO_2/ 90.3% N_2	22	4.0	0	5.5	13.8	0	0	0
13	13.4% CO_2/ 86.6% N_2	24	5.5	0	6.0	10.9	0	0	0
14	12.3% CO_2/ 87.7% N_2	26	5.0	0	6.0	12.0	0	0	0
15	12.4% CO_2/ 87.6% N_2	28	5.3	0	6.1	11.5	0	0	0
16	5.0%/12.7%/ 82.3% N_2	28	2.0	5.2	3.1	15.5	4.7	0	11.8
17	9.6%/16.0%/ 74.4% Ar	20	3.9	6.5	2.8	7.2	0	0.07	0
18	8.3%/ 13.5%78.2% Ar	28	3.4	5.5	2.7	7.9	0	0.05	0

Table 1 continued

	Composition $CO_2/CH_4/N_2$ or Ar	Power/ W	$[CO_2]_{feed}/10^{-3}$M	$[CH_4]_{feed}/10^{-3}$M	Gain CO/ 10^{-4}M	%CO	Gain HCN/ 10^{-4}M	Gain HCHO/ 10^{-4}M	Abs 2152 $cm^{-1}/10^{-3}$
19	54.0%/18.0%/ 28.0%	28	22.0	7.3	8.8	4.0	0	0	0

Abs 2152 cm^{-1} is the absorbance of the ketene band after subtracting the absorbance of CO, and %CO is the percentage of the CO_2 feed converted to CO, see text for details. Rows 1a, b, 3a and b and 5a and b show duplicate experiments carried out several months apart. ? indicate experiments in which the formaldehyde absorption could not be discerned clearly, e.g. due to overlying water bands due to adventitious water vapour

beam was incident on the sample in the cell at angles from 20° to 76° with respect to the horizontal plane via a ZnSe window.

Data Manipulation

The spectra obtained in the thermally-driven and plasma-driven experiments are presented as:

$$\text{Absorbance, } A = \log_{10}(S_R/S_S) \tag{2}$$

This results in difference spectra in which peaks pointing upwards (i.e. to + absorbance) represent a gain in absorbing species at S_S with respect to S_R, and peaks pointing down (to − absorbance) represent the loss of absorbing species. The concentrations of the various species observed in the plasma experiments were calculated using the Beer–Lambert law:

$$A = \varepsilon cL \tag{3}$$

where ε is the molar decadic extinction coefficient (M^{-1} cm^{-1}), c concentration (M) and L optical path length (cm).

The conversion of CO_2 to CO is:

$$\%CO = 100 \times [CO]_{glow} \Big/ [CO_2]_{glow} \tag{4}$$

The energy efficiency for the production of CO is:

$$\eta_{CO}/\% = 100\Delta H^0/E_{pCO} \tag{5}$$

where ΔH^0 is the enthalpy (279.8 kJ mol^{-1}) of the process:

$$CO_2 \rightarrow CO + {}^1\!/_2O_2 \tag{6}$$

at 300 K [40]. $E_{p\ CO}$ is the energy expended in producing 1 mol of CO and assuming that the IR spectra record an average picture over the 1 min data collection time.

The errors inherent in the calculations involving the integrated areas of the CO_2 etc. features are detailed in the previous paper [37].

Results

Figure S2 shows a spectrum taken before the 24 W run of the 8.5% CO_2 + 13.1% CH_4 + 78.4% N_2 feed gas without plasma at a total flow rate of 200 cm^3 min^{-1}, referenced to N_2 gas at the same flow rate, at 25 °C. The intense feature between 2300 and 2400 cm^{-1} is due to the P and R bands of the CO_2 asymmetric stretch (ν_3) fundamental absorption [41, 42] and the features between 3500 and 4000 cm^{-1} are CO_2 combination bands ($\nu_1 + \nu_3$ and $2\nu_2 + \nu_3$) [43]. It is clear from the figure that the fundamental bands are saturating and hence cannot be employed for any quantitative measurements; hence it was decided to employ the integrated areas of the CO_2 combination bands between 3491 and 3769 cm^{-1} to estimate the CO_2 conversion, the absorption coefficient employed was 6.5×10^5 cm mol^{-1} [37]. Using the thermal FTIR system, it was found that this value remained constant over the temperature range from 25 to 150 °C [37].

The bands with Q branches centred at 3017 and 1302 cm^{-1} may be attributed to the P, Q and R branches of the ν_3 and ν_4 fundamentals of CH_4, respectively [42]. Using a 1 cm pathlength gas cell [37] and 100% CH_4, the extinction coefficients at 3086 and 1346 cm^{-1} were determined as 3.5 ± 0.4 and 6.4 ± 0.1 M^{-1} cm^{-1}, respectively. These values were checked using a 0.6 cm pathlength cell.

Figure 1 shows the spectrum collected after 2 min at 24 W and the spectrum collected of the same $CO_2/CH_4/N_2$ feed gas with no plasma, both using the nitrogen single beam spectrum as reference. Bands due to HCN and CO were observed and are discussed below. After 2 min plasma operation, although the features other than HCN and CO appear to be due to room temperature CO_2 and CH_4 bands they are all marginally broader and the Q branches of the ν_4 and ν_3 bands of CH_4 are also shifted slightly. This can be seen more clearly in Fig. S3(a) which shows the spectrum in Fig. 1 using the single beam spectrum collected with no plasma but with the same feed gas (8.5% CO_2, 13.1% CH_4 78.4% N_2), i.e. Fig. S3(a) is a difference spectrum. The broadening of the various features in Fig. 1 compared to the room temperature absorptions of the feed gases can be seen in Fig. S3(a) as the gain of "wings" either side of the CO_2 and CH_4 loss features, the much reduced fine structure on the ν_4 band and, in the case of the Q branches of the CH_4 bands, as significantly reduced absorptions and the bipolar nature of the ν_3 Q branch. The ν_3 band of CH_4 and the asymmetric CO_2 stretch were simulated using Spectralcalc and the difference spectra obtained by subtracting the room temperature spectra from those at 396 K are shown in Figs. S3(b) and (c): thus we assign the gain features in Fig. 1 for CO_2 (CO_2*) [30, 44] and CH_4 (CH_4*) to those due to higher temperatures in the plasma leading to increased rotational excitation.

There is no evidence of non-thermal vibrational excitation enhancement. This is supported by the experiment carried out using the thermal FTIR system, see below.

Figure 2 shows spectra collected after 20 min running with plasma at 20, 24 and 28 W, all using the spectra collected with the same gas feed but without plasma as the reference spectra. As can be seen, in addition to CO_2* and CH_4*, other species were clearly produced in both liquid and gas phases: with respect to the former, a pale brown liquid was found to coat the internal walls and windows of the cell and subsequent experiments (see below) showed this to be composed of a number of species. It was decided to obtain a spectrum of the liquid: thus Fig. S4 shows the spectrum collected after 20 min at 24 W in Fig. 2 along with the spectrum collected at the end of the same experiment after the cell had been purged with N_2 to remove all gas phase species: the latter spectrum was thus of the liquid film on the CaF_2 windows. The spectrum taken after 20 min operation had that taken after

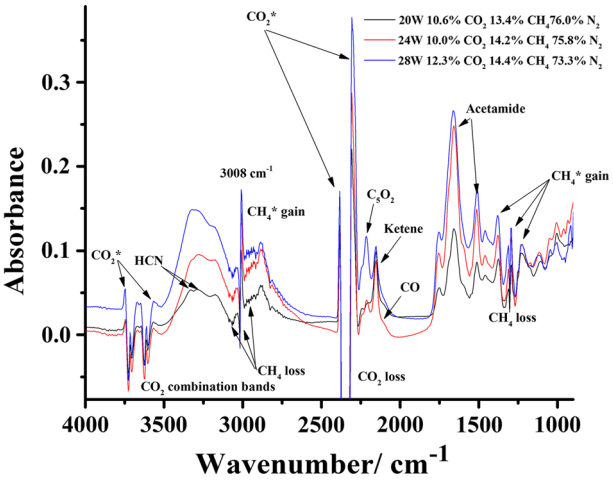

Fig. 2 In-situ FTIR spectra (8 cm^{-1} resolution, 100 spectra per scan set, and 1 min per spectrum) collected after 20 min operation with plasma as a function of input power. The gas compositions are as shown on the figure at a total flow rate of 200 cm^3 min^{-1} and a temperature of ca. 25 °C; the reference spectrum was collected under the same conditions but with no plasma. Sample spectra were collected every 2 min up to 20 min

2 min subtracted: the reason for this can be seen in Fig. 2, where the peaks between 2000 and 2250 cm^{-1} in Fig. 2 are overlying the P and R bands of gas phase CO (see below) which remain essentially unchanged with time, indicating that the CO rapidly attains a steady state concentration: this is also the case for HCN, these observations are discussed further below. By subtracting the spectrum taken after 2 min, the features between 2000 and 2250 cm^{-1} were clearer, and this approach was adopted below. The IR spectra obtained at an input power of 24 W were typical of those obtained at 20, 22, 26 and 28 W, differing only in the relative intensities of the various features.

The 1655 cm^{-1} band is directly associated with one or more of the components of the liquid film: as can be seen in Fig. 2, the exact position of the band maximum and the peak shape varied from experiment to experiment suggesting contributions from more than one species however, for clarity, it is referred to as the 1655 cm^{-1} band in the discussion below. As may be seen from Fig. S4, as well as the liquid film (represented by the 1655 cm^{-1} band), gaseous products were observed, one of which showed a strong absorption at 2152 cm^{-1} which consistently decreased in intensity when the cell was sparged with N_2. We attribute this absorption to ketene [45, 46], a carbon chain oxide; we also attribute the band at 2210 cm^{-1} in Figs. 2 and S4 to another carbon chain oxide, C_5O_2 [47–49] which is a liquid at room temperature, hence its presence in the deposit [50]. This is an important observation: the production of neither ketene nor C_5O_2 has been observed previously in NTP experiments irrespective of the nature or composition of the catalyst or dielectric, and this was achieved by using a catalyst comprised of earth-abundant elements. Further, ketenes and their dimers are important reactants that find use in the production of a wide range of chemicals [51–53] in a diverse range of industries including pigments, pharmaceuticals and agrochemicals and as intermediates for the paper industry. The 2152 and 2210 cm^{-1} bands are in a distinctive spectral region that is populated by relatively few functional groups: in addition, their intensities do not, in general, track those of the other bands in Figs. 2 and S4, lending support to their identification as chain oxides. Further,

ketene has been observed in a matrix FTIR study of products of benzene transformations in a pulsed glow discharge at low pressure in highly diluted mixtures of benzene with argon in the presence of small amounts of oxygen [54]. As an interesting aside, the observation of the production of ketene and C_5O_2 in a non-thermal plasma catalysed by common elements has direct relevance to the origin of life: e.g. C_5O_2 is a powerful tracer of the temperature history of formerly carbon monoxide rich ices in molecular clouds and star-forming regions [55] and ketene is one of the Complex Organic Molecules (COMs) formed in prestellar cores [56].

It is interesting to note from Fig. 2 that the relative yield of ketene and C_5O_2 depends strongly on the input power, whilst the production of the liquid film does not appear to be so dependent; this suggests one method of potentially controlling the product distribution from the plasma process.

The Spectra Collected After 2 min

Figure 3 shows the spectra collected after 2 min of plasma operation at 28 W in the experiments shown in Fig. 2 and analogous experiments carried out at the same input powers with varying gas feed compositions. The bands at 3334 and 3286 cm^{-1} in Fig. 3 were attributed to the P and R branches of HCN based on the work of Choi and Barker [57]; the paper also allows an estimate of the extinction coefficient of the 3334 cm^{-1} band of 2.8 M^{-1} cm^{-1}.

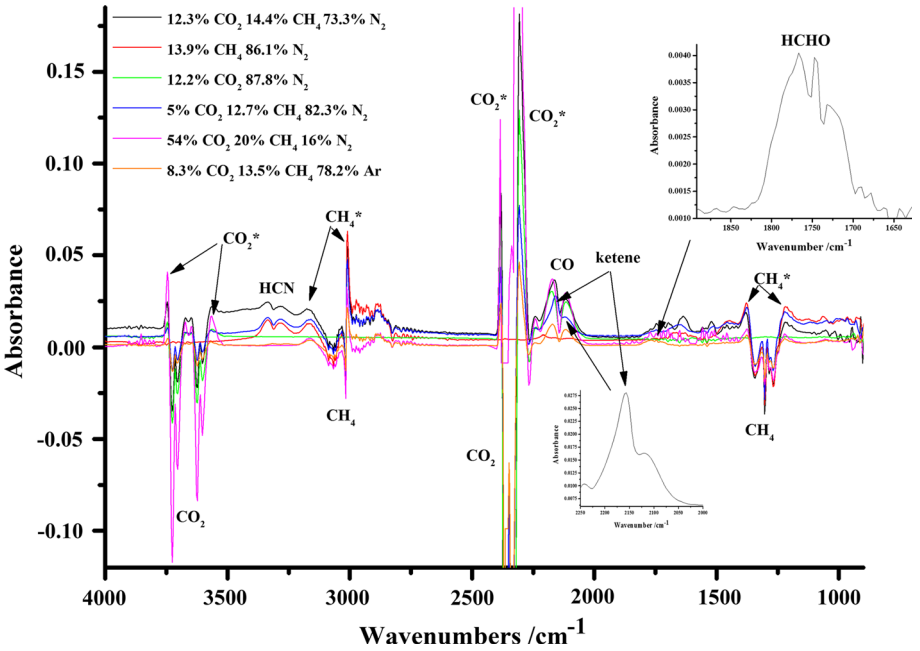

Fig. 3 The spectrum collected after 2 min of plasma operation at 28 W in Fig. 2, along with analogous experiments using gas feeds of various composition, as shown on the figure. The insets show the spectral regions where formate and ketene absorb in the experiment carried out using 5.0% CO_2 + 12.7% CH_4 + 82.3% N_2

The features at 2167 and 2116 cm^{-1} in Fig. 3 may be attributed to CO [37, 42, 58]: the frequency of the former, in some cases, shifted by the presence of an underlying absorption, as shown by the inset of the spectrum from the experiment using 5.0% CO_2 + 12.7% N_2 + 82.3% N_2 in the figure. Fig. S5 shows the CO region of the spectrum collected at 2 min and 24 W in the experiment in Fig. 3, as well as that of a spectrum collected after 2 min operation at 24 W in 13.4% CO_2 86.6% N_2, the latter was reduced by a factor of 1.3 to render the 2116 cm^{-1} bands the same intensity. The figure also shows the spectrum resulting from the subtraction of the CO_2 + N_2 spectrum from that of CO_2 + CH_4 + N_2: clearly, the CO bands are of the same intensities and frequencies, with the difference due to the presence of the 2152 cm^{-1} ketene feature. Using the 1 cm pathlength cell, the integrated absorption coefficient of the CO band between 2002 and 2225 cm^{-1} was found to be 7.0 × 10^5 cm mol^{-1} in agreement with the work of Bolis and et al. [59].

Figure S6 which shows the spectra collected after 2 min in experiments utilising the feed gas compositions and input powers shown in rows 1a, b, 3a, b and 5a, b of Table 1 (i.e. nominally 10% CO_2 + 10%CH_4 + 80%N_2 at 20, 24 and 28 W) and that taken after 2 min during the experiment using 5.0% CO_2 + 12.7% CH_4 + 82.3%N_2 as feed gas (row 16), with the analogous spectra obtained using CO_2 + N_2, scaled and subtracted to annul the CO absorptions in each spectrum; the intensities of the ketene band so obtained are presented in the last column of Table 1 which summarizes the data obtained from the experiments in Fig. 3 along with data obtained in analogous experiments carried out as blanks (omitting CO_2 or CH_4), replacing N_2 with Ar and to probe the effect of input power, etc. The spectra from the blank experiments are not included in this work for brevity: the experiments using CO_2 alone as the feed gas have been fully described in the previous paper [37], and those using CH_4 will be described in detail in later publications. It is very clear from the table that the production of ketene (and indeed the liquid products seen at longer times, see below) requires all three gases. Further, at fixed composition, the gain of ketene increases with input power. This may be due to the formation of the methyl radical from CH_4 as the first intermediate in the production of ketene (see Scheme 1): CH_3 is known to be an important intermediate for example in the formation of acetic acid from CO_2 and CH_4 [60].

The second inset on Fig. 3 shows the spectral range between 1640 and 1900 cm^{-1} of the experiment using 8.3% CO_2 + 13.5% CH_4 + 78.2% Ar: the feature may be attributed

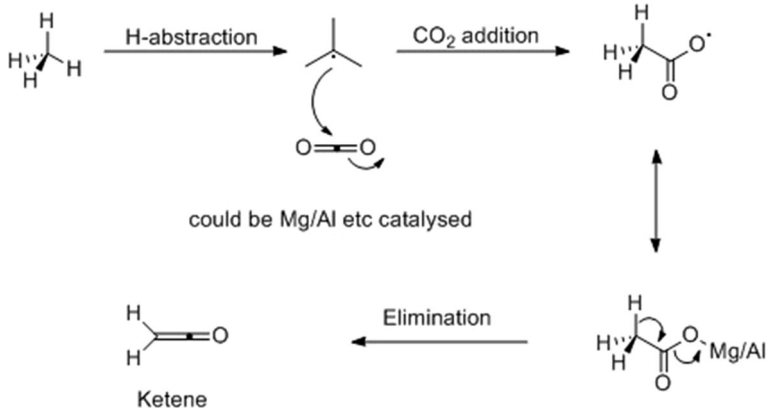

Scheme 1 Possible mechanism for the formation of ketene at Macor

to the P, Q and R branches of the ν_2 fundamental absorption of formaldehyde [42, 61]. The integrated extinction coefficient of formaldehyde over the range 1660–1820 cm^{-1} is ca. 1.25×10^{-17} cm mol^{-1} [62] and this was employed to calculate the concentration of formaldehyde in the plasma glow region.

It is clear from Fig. 3 and Table 1 that there is some conversion of CO_2 and CH_4 to CO, HCN and formaldehyde after 2 min, but that the major fraction of the reactant gases remain unreacted and present at an increased gas kinetic temperature with broadening due to higher rotational excitation as a result of the higher gas temperature: this is a reasonable assumption for atmospheric pressure. In the absence and presence of CH_4, the conversion of CO_2 to CO (rows 1–5 and 11–15 in Table 1) appears to be largely independent of input power, which is unexpected as the mean electron energy increases with power, and hence more conversion would be expected. The conversions in CO_2/N_2 are comparable to those in $CO_2/CH_4/N_2$ suggesting that CH_4 played no part in the reduction of CO_2 to CO. This is because the main process is a single step electron dissociation of CO_2.

Increasing the dilution of the CO_2 by N_2 and $N_2 + CH_4$ (rows 16, 5a, b, 15 and 19) reduced the conversion of CO_2 to CO by a factor of 4: i.e. from 15.5% at 5.0% CO_2 to 4% at 54.0% CO_2. Xu et al. [63] interpret such behaviour in terms of an increase in the number density of higher energy electrons in CO_2 non-thermal plasma on dilution with N_2 or Ar. The mean electron energy per molecule ranges from 3.9 to 5.5 eV at the lowest and highest input energies employed by us: given that the threshold energies for the excitation and ionization of CO_2, N_2, CH_4 and Ar are all significantly above these values [64–67], see Table 2, this suggests that electrons in the high energy tail of the distribution must play a significant role.

When N_2 was replaced by Ar, the input power had little or no effect (rows 17 and 18), neither did changing the feedgas at 20 W. However, at 28 W, the conversion to CO was reduced by ca. 36%. The latter effect is unsurprising as the ionization energy of Ar is high, 15.76 eV [68] and it is generally accepted that, at the high concentrations of N_2 employed (70–90%), metastable N_2 states will be primarily responsible for the conversion of both CO_2 and CH_4 [64, 68]:

$$N_2\left(A^3\sum_u^+\right) + CO_2 \rightarrow CO + O + N_2 \tag{7}$$

and the Penning dissociation of CH_4:

$$N_2\left(A^3\sum_u^+\right) + CH_4 \rightarrow CH_3 + H + N_2 \tag{8}$$

Table 3 shows the calculated mean electron energies for different compositions of $CO_2/CH_4/N_2$/Ar assuming a reduced electric field, Td, of 200 and a temperature of 300 K using BOLSIG + [69]. The first excitation threshold of N_2 is 7.7 eV (see Table 2) and the

Table 2 Electron impact excitation and ionization threshold energies [63–65, 67]

Species	Excitation threshold/eV	Ionization threshold/eV
CO_2	6.2	13.8
CH_4	10	12.65
Ar	11.5	15.8
N_2	7.7	14.5

Table 3 Mean electron energies for different percentage compositions calculated from BOLSIG + [69] at a reduced electric field of 200 Td and a temperature of 300 K

CO_2	CH_4	N_2	Ar	Mean electron energy/eV
100	0	0	0	5.896
0	100	0	0	5.523
0	0	100	0	5.056
0	0	0	100	7.905
50	50	0	0	5.612
25	25	0	50	6.521
25	25	50	0	5.409

electron energy distribution of our system possesses a significant population with energy greater than this and so this mechanism is feasible in our plasma cell.

In the absence of CO_2, 9–12% of the CH_4 (rows 6–10) was converted to HCN. Although HCN is not a desired product, the presence of HCN shows that nitrogen fixation has occurred and it is produced in comparable quantities to CO, so its origin is of interest: as would be expected, CH_4 is clearly essential for its formation, but a comparison of rows 1–5, 6–10, 16 and 19 strongly suggests that CO_2 suppresses this process, due to the production of reactive O atoms favouring the oxidation pathways. The production of HCN increased with input power (see rows 1–5) in the presence of CO_2 and CH_4, but showed no dependence upon power in the experiments using just CH_4 and N_2 (rows 6–10). The study of the plasma driven conversion of CH_4/N_2 mixtures is topical due to their relevance to the atmospheres of Titan and Triton (and the postulate that these are models for the early development of Earth) [70–72] and also with respect to natural gas conversion [73]. Horvath et al. [72] have observed HCN at similar concentrations using the same SIE as here: thus the authors employed a cylindrical, co-axial quartz reactor packed with borosilicate beads and supplied with 10%CH_4/N_2 at SIEs of 1–30 kJ dm^{-3}. At an SIE of ca. 8.4 kJ dm^{-3} the authors observed 10,500 ppm HCN in the exhaust from the reactor, ca. 5×10^{-4} M and comparable to the 6.0×10^{-4} M observed by us in the plasmaglow at the same SIE. Horvath et al. postulated that the formation of HCN occurs via the reaction of CH_x radicals with N atoms: however, the dissociation energy of N_2 is 9.756 eV [74] and the authors observed HCN at SIE as low as 1 kJ dm^{-3}, equivalent to an average electron energy per molecule of 0.25 eV for a uniform electric field. However, in the packed bed plasma configuration enhanced electric fields are likely to arise between the beads leading to higher electron energies [60]. The high energy part of the electron energy distribution function is thus likely to be able to directly dissociate N_2.

The gas phase production of HCN in the plasma region is most likely produced by the following mechanism [72]. the initial step is electron impact reaction with CH_4 which requires electron energies greater than 10 eV. The CH_x radicals can then react further with N to produce HCN:

$$CH_4 + e^- \rightarrow CH_3 + H$$
$$CH_4 + e^- \rightarrow CH_2 + H_2$$

Followed by:

$$CH_3 + N \rightarrow HCN + H_2$$
$$CH_3 + N \rightarrow H_2CN + H$$
$$CH_2 + N \rightarrow HCN + H$$
$$CH_2 + N \rightarrow CN + H_2$$
$$H_2CN + N \rightarrow HCN + NH$$
$$CN + CH_4 \rightarrow HCN + CH_3$$
$$H_2CN + H \rightarrow HCN + H_2$$

In contrast, Snoeckx et al. [73] in their cylindrical reactor without packing observed HCN at concentrations an order of magnitude lower than ourselves and Horvath: e.g. at 6 kJ dm^{-3} using N_2 concentrations from 1 to 87% Snoeckx et al. observed HCN at concentrations from 4.0×10^{-7} M to 1.7×10^{-5}M, respectively. The authors attributed the very low HCN production to the fact that the SIE was lower than required to generate N_2^+ which the authors and others have postulated ([73] and refs therein) are the intermediates in the formation of HCN [72], e.g.:

$$N_2\left(X^1\sum_g^+\right) + e^-(15.63\ eV) \rightarrow N_2^+\left(X^2\sum_g^+\right) + 2e^- \quad (9)$$

However, it is not clear from the cited papers how N_2 is an intermediate in the formation of HCN.

As stated above, in our case, there was no clear relationship between the concentration of HCN in the plasma glow and the SIE: this and the lower dissociation energy of N_2 favours the mechanism proposed by Horvath et al.

Interestingly, when N_2 was replaced by Ar (Table 1, rows 17 and 18), a new absorption appeared with branches at 3315 and 3263 cm^{-1} which we attribute to acetylene [42], see Fig. S7.

In general, η_{CO} was ca.1–3%, which is in broad agreement with the literature where efficiencies are generally quoted as $\leq$ 10% [65]: in addition, the cell was designed to allow spectroscopic monitoring of the plasma, rather than to maximize conversion efficiencies.

We estimate that bands due to O_3, NO_2 and N_2O at 1051, 1628 and 2237 cm^{-1} [44] having absorbances of 0.02 would be easily discerned in the spectra in Fig. 2: using the reported extinction coefficients for these species [44], we estimate therefore that if they are present it is at concentrations $<$ ca. 10^{-5}M.

The Spectra Collected at Later Times

In order to maximize the peak intensities observed, the spectra collected during the experiment carried out at 28 W were selected for further study. In addition, given that the HCN and CO bands in general did not change with time in any of the experiments, the spectrum collected after 2 min at 28 W was subtracted from the spectra collected at later times, and the results are shown in Fig. 4. The loss and gain features in the CH_4 and CO_2 regions of the figure reflect the increased gas kinetic temperature of these species with time: in other words, the loss features are due to the less rotationally excited species. The HCN and CO bands are clearly absent, showing that these species had reached steady state concentrations in the plasma by 2 min. Plots of the various features in Fig. 4 are shown in Figs. 5a and b, and the analogous plots for the experiments carried out at the other input

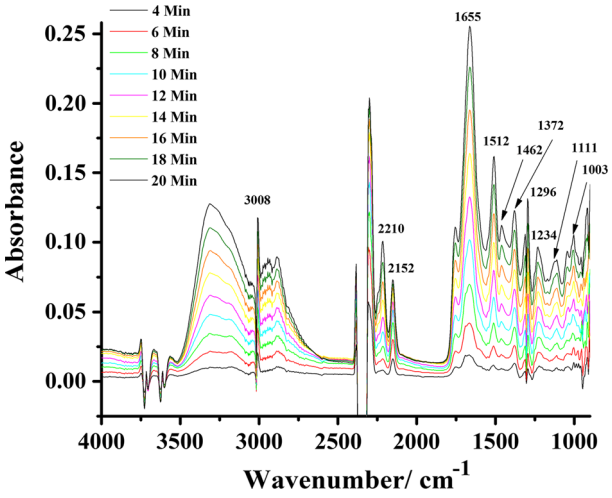

Fig. 4 In-situ FTIR spectra (8 cm^{-1} resolution, 100 spectra per scan set, and 1 min per spectrum) collected as a function of time at a fixed input power of 28 W. The gas composition was 12.3% CO_2 + 14.4% CH_4 + 73.3% N_2 at a total flow rate of 200 cm^3 min^{-1} and a temperature of ca. 25 °C; the reference spectrum was collected under the same conditions but with no plasma. Spectra were collected every 2 min up to 20 min. The spectrum collected at 2 min was subtracted from those taken at longer times, see text for details

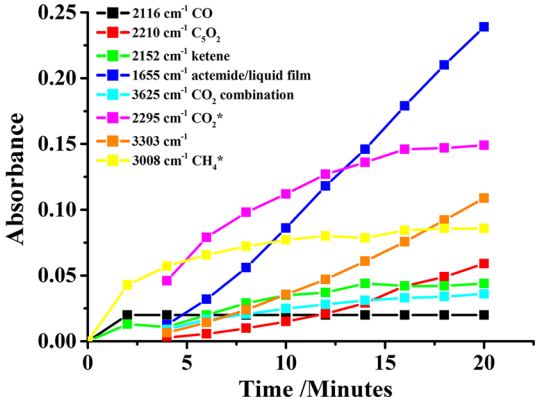

Fig. 5 **a** Plots of the intensities of the various features in Fig. 4 as a function of time. **b** The plots in **a** normalised to their maximum values

powers, are shown in Figs. S8(a)–(d). The absorbance at 2295 cm^{-1} on the wing of the CO_2* feature was taken as an indication of the increasing rotational excitation with temperature. Figure 5a shows plots of the band intensities as a function of operation time and Fig. 5b the corresponding plots of the intensities normalised to their maximum values. The plots of CO intensity at 2116 cm^{-1} were calculated with respect to the reference spectrum taken with no input power, all other features were calculated from the difference spectra, with the spectrum collected at 2 min subtracted: the plots of the normalised intensities of the CO band can also be taken as representative of HCN.

It is clear from Figs. 4, 5a, and S8(a)–(d) that the intensities of the various features observed show that the species responsible show three types of behaviour: HCN and CO rapidly attain a steady state irrespective of the formation of the liquid film, suggesting these take place entirely in the plasma region. The CO_2, CO_2* and 2152 cm^{-1} ketene bands show a rapid initial increase which tails away at longer times, but their concentrations in the plasma continue to grow: in contrast, the 2210 cm^{-1} C_5O_2, 1655 and 3303 cm^{-1} bands take longer to develop and then increase fairly steadily. This suggests that the three types of behaviour are due to species produced or consumed by three distinct processes although

links between them may also be present. From Fig. 4, it appears that the broad gain feature between 2500 and 3500 cm^{-1}, which is distorted somewhat by ν_3 CH_4* absorptions, is due to the same species as the 1655 cm^{-1} feature and this was confirmed by plotting the intensities of the two features against each other, see Figs. S9(a)–(c) for the experiments conducted at input powers of 20–28 W (only the data for 20, 24 and 28 W are shown for clarity). The same procedure confirmed that the 1512 cm^{-1} band was also due to this species. A clue to the identity of this species was provided by the lack of any intense bands due to C-H stretches in Figs. 1, 3, 4 etc., along with the broad absorption between 2500 and 3500 cm^{-1} which appeared to comprise two bands. On the basis of the literature [42, 75, 76], we attribute the broad feature between 2500 and 3500 cm^{-1} to the N–H stretch of acetamide, the weak 2880 cm^{-1} band to the asymmetric C–H stretch and the 1655 and 1512 cm^{-1} bands to the amide I (C=O stretch) and amide II (N–H in plane deformation), respectively. As well as the carbon chain oxides, acetamide is also important to the study of prebiotic life as it is the largest interstellar molecule bearing the critical amide functionality [77].

The 1655 cm^{-1} feature also has contributions from the in-plane N–H bend, C-N stretch and C–C–N deformation. This is clearly not the only species present in the liquid film which shows a plethora of clearly defined (but as yet unidentified) bands below 2000 cm^{-1} as well as a significant broad underlying absorption suggesting a number of overlapping bands. Further, the liquid film is a yellowish colour suggesting, for example, conjugated C=C and C=N bonds. The postulate that the 1655 cm^{-1} band is a composite of a number of absorptions is supported by close inspection of the spectra collected after 4 and 20 min in Fig. 4, where it can be seen that the absorption around 1655 cm^{-1} in the 4 min spectrum comprises a number of peaks.

Figure 6 shows preliminary data obtained using the reflectance cell shown in Fig. S1(b) during a repeat of the experiment in Fig. 2 experiment in which spectra were collected every 2 min after initiating the plasma at an input power of 24 W. The figure shows the spectrum collected after 20 min plasma operation and the spectrum of the deposit which remained after 10 min flushing with N_2. As a result of the shorter pathlength

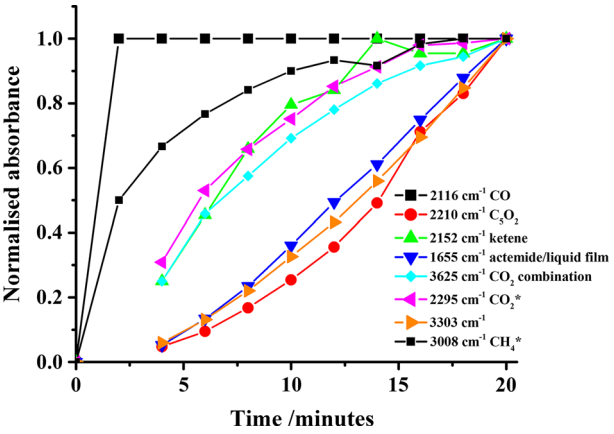

Fig. 6 (i) Spectrum of the liquid deposit formed on the CaF_2 windows of the transmission following a repeat of the experiment at 24 W in Fig. 2. At the end of the experiment, the cell was flushed thoroughly with N_2 and a spectrum collected using the spectrum taken of the cell containing nitrogen prior to the experiment as the reference. (ii) Spectrum of the liquid deposit on the CaF_2 window of the reflectance cell following an analogous experiment at 24 W to that depicted in Fig. 2. See text for details

of the reflectance cell (1 cm), the CH_4 ν_4 bands are much weaker, revealing underlying absorptions due to the components of the liquid film: thus there are additional features at 1300 cm^{-1} (the 1296 cm^{-1} band in Fig. 4 perturbed by the loss features due to CH_4*) and 1016 cm^{-1}. In contrast to all the spectra observed using nominally the same feed gas composition in the transmission cell, where the 1752 cm^{-1} feature is relatively weak, this band is comparable in intensity to the feature at 1655 cm^{-1} in Fig. 6. The spectrum collected using the reflectance cell includes information from both the window and the Macor, in contrast to the transmission cell spectrum which only shows the deposit on the windows of the cell. Further, the reflectance cell has one exposed Ti mesh electrode. This suggests that the 1752 cm^{-1} feature may be attributed to a species present in a higher amount at the Macor/Ti mesh than on the CaF_2 window, and that this may be produced as a result of contact of the plasma with the mesh. That the Macor and/or Ti are contributing to the spectrum in Fig. 6i is shown by the bands at 1150 and 1219 cm^{-1}. As may be seen, both features decreased in intensity as the cell was flushed with N_2: however, the latter band ceased to decrease, and changed structure. This was due to the presence of two bands, one at ca. 1228 cm^{-1} (correlating with the 1234 cm^{-1} feature in Fig. 4) due to the liquid film and a second, at 1210 cm^{-1} that increased in intensity in concert with the 1150 cm^{-1} band. The 1150 and 1210 cm^{-1} bands are associated with the Ti/Macor surface, as they appear in experiments using pure N_2 as the feed gas, see Fig. S10. They were induced by the plasma and relaxed slowly, i.e. over many minutes, when the plasma is turned off. We have been unable to identify the species responsible for these absorptions to date and, whilst interesting, it is not clear that these species participate in the processes observed and hence are not relevant to the aim of this paper. Further work is in progress to elucidate this chemistry, and will be reported in a future publication.

Figure 7 compares the spectra obtained after 20 min at an input power of 28 W with the corresponding spectra collected after 2 min subtracted using feed gas compositions selected to investigate the effect of CO_2 and N_2. It is clear that excess CO_2 or replacing N_2 with Ar both prevent the production of the chain oxides and the liquid film, despite the

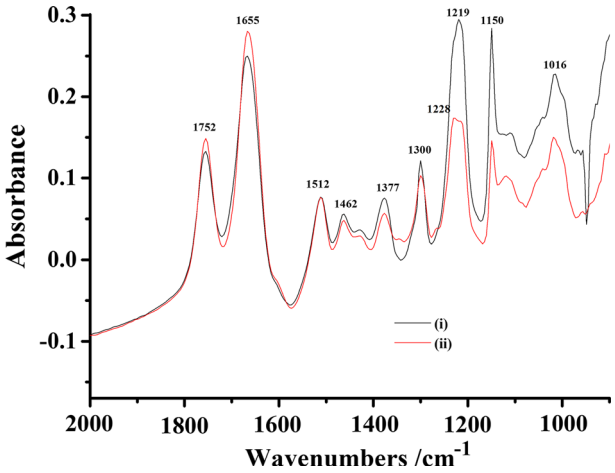

Fig. 7 In-situ FTIR spectra (8 cm^{-1} resolution, 100 spectra per scan set, and 1 min per spectrum) collected after 20 min operation at input power of 28 W as a function of the gas compositions shown on the figure. In each case, the corresponding spectrum collected after 2 min operation was subtracted. Total flow rate was 200 cm^3 min^{-1} the temperature ca. 25 °C

presence of methane in both cases. Thus the feed gas composition has a major effect upon the products observed. The relative absorbances of the various hot CO_2 and hot CH_4 features essentially reflect the initial concentrations of the ground state species in the feed gas.

A summary of all the assignments is presented in Table 4.

Thermal Experiments

Figure S11 shows the spectrum collected at 100 °C during an experiment in which the reference spectrum was collected at 25 °C and the temperature increased in steps up to 600 °C, with further spectra collected at each step. The spectra were collected from the Macor disc in 43% CH_4 21% CO_2 36% N_2 in the sealed system (i.e. batch mode). It is clear from the figure the same features are observed in the ν_3 and ν_4 regions of the CH_4 absorption and either side of the fundamental absorption of CO_2 as in the plasma experiments, supporting the assignments to CH_4* and CO_2*. No other products were observed up to 600 °C, clearly showing that catalyst selection for plasma driven systems cannot be based solely on materials that work in thermally-activated processes.

Table 4 A summary of the assignments of the various features in Figs. 2, 3, and 4. See text for details

Peak/cm^{-1}	Assignment
3017	Q branch of ν_3 band of CH_4
1302	Q branch of ν_4 band of CH_4
3726	Combination bands of CO_2
3704	
3625	
3600	
2167	P branch CO
2116	R branch CO
3334	P branch HCN
3286	R branch HCN
2210	C_5O_2
2152	$H_2C{=}C{=}O$, ketene
ca. 1767	P branch HCHO
1745	Q branch HCHO
ca. 1724	R branch HCHO
ca. 3303	N–H stretch of acetamide and underlying liquid film absorption
2880	Asymmetric C–H stretch of acetamide
1655	Acetamide I and underlying liquid film absorption
1512	Acetamide II and underlying liquid film absorption

Discussion

Both plasma cells are flow systems i.e. reactants were constantly supplied and products removed: however, the plots in Figs. 4, 5a, b and Figs. S8(a)–(d) show that the concentrations of CO_2* and CH_4* change relatively little with time, whilst the concentration of ketene in the plasma, and C_5O_2 in the liquid film increase. Given that the input power and flow rate did not vary during the experiments, this suggests that the rate of formation of these products increased with time, whilst the rates of formation of HCN and CO (and possibly formaldehyde) remained constant. As stated above, this suggests parallel and separate reaction pathways: in addition, the data indicate that some aspect of the system is changing and steadily increasing the rate of formation of ketene etc. A logical postulate would be the increasing build-up of reactive intermediates on the Macor surface: e.g. magnesium carboxylate and magnesium nitride, see Schemes 1 and 2. The higher chain oxide C_5O_2 could then be produced via the reaction of methane and ketene according to:

$$CH_4 + 2H_2C = C = O \rightarrow C_5O_2 + 4H_2 \quad (10)$$

However, in all the 20 min experiments discussed above, the reactions near to the Macor proceeded and indeed accelerated, as the liquid film formed. In contrast, by the end of a two-hour experiment, using essentially the same feed gas composition as that in Fig. 4 and 28 W input power, the production of all the species observed in Fig. 4 had ceased, presumably as the Macor was completely covered, or covered beyond a maximum thickness of the liquid film: the latter possibility arises due to the fact that in all the experiments employing the nominal gas feed composition to the naked eye both the Macor caps were covered with the liquid film after only 20 min plasma operation. Thus, it does not seem unreasonable to postulate that, at thicknesses lower than some critical maximum, the film facilitates the production of the ketene and C_5O_2: for example, it has been reported that the penetration depth of electrons into an aqueous solution is ca. 12 nm [78]: in our case, the third reaction zone could be a layer within the liquid droplets defined by the penetration depth of the electrons, analogous in some ways to the catalysis taking place at the boundary between metal particles and oxide substrates [79]. Above the critical maximum thickness,

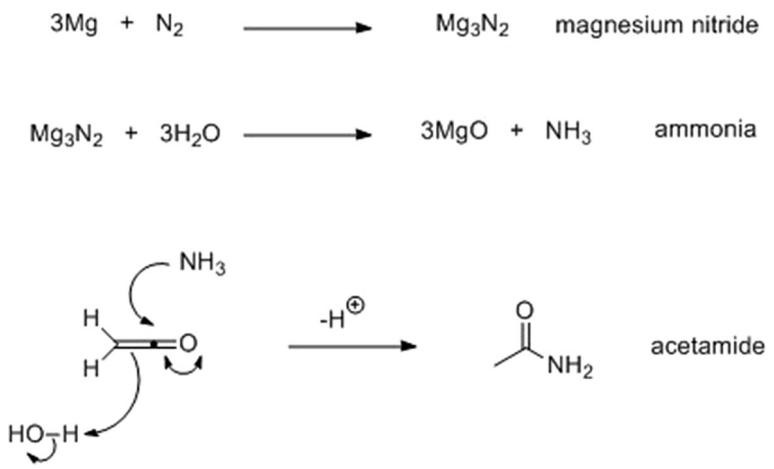

Scheme 2 Possible mechanism for the formation of acetamide

defined presumably by the dielectric constant of the liquid film, the electric field decreases below that necessary to sustain the plasma.

Our data thus suggest the presence of at least two reaction zones: one at the Macor/-plasma interface and one that is the plasma bulk. A third zone involves the liquid, perhaps at its boundaries. This model is a development of the two-zone model proposed by Kim et al. [80] in which the active species in the plasma such as OH radicals and ground state O atoms occupy a thin layer perhaps 50 μm thick above the catalyst and are available for reaction at the catalyst: above this layer, species produced in the plasma react in the same way as in the absence of catalyst. Our model is supported by an experiment in which isoprene was added to 11.0% CO_2 + 15.0% CH_4 + 74.0%N_2 in an attempt to trap ketene via a cycloaddition reaction [81]: instead, whilst CO_2*, CO and HCN were still observed, wholly different liquid products were produced, the spectrum of which was identical to that reported by Scarduelli et al. [82], see Fig. S12, and the isoprene simply polymerized on the Macor caps. Scarduelli et al. employed a conventional NTP tube reactor fed with a 60:40 mixture of CH_4 and CO_2 (no nitrogen); both electrodes of the reactor were isolated from the plasma by silica glass such that the plasma contacted only silica. Our data and the results of Scarduelli et al. strongly suggest that the polymerization of the isoprene on the Macor essentially masked its catalytic properties and the reaction zone was thus confined to the plasma itself. In other words, the presence of the Macor is essential for the specific liquid film composition obtained in our experiments discussed above, nitrogen is required to activate the Macor and the liquid film then has a direct influence on the production of ketene and C_5O_2, for example either by providing a liquid reaction zone where reactants/reactive intermediates can be concentrated, or by acting as a catalyst.

The chemical species observed here, namely: CO, HCN, HCHO, CH_2CO, C_2O_5, and acetamide are very much a subset of the product species expected in the dry reforming reaction. H_2 is one of the main products but could not be observed by our FTIR detection methods. However it would have been expected to observe hydrocarbons: C_2H_6, C_2H_4 and C_2H_2 which were either obscured in the spectra and/or below our detection limits. The one-dimensional fluid model for a typical DBD plasma reactor for CO_2/CH_4 by de Bie et al. [16] predicts these species as products but in our case with added N_2 the routes to C2 species may be diverted by reaction with N atoms to preferentially form HCN. It is interesting that de Bie et al. also predict ketene (CH_2CO) but did not include C_2O_5 in the calculation. As far as we are aware, this is the first time that it has been observed in dry reforming reactions.

Conclusions

Macor contains the oxides of the earth-abundant elements Mg, Al and Si: despite its relatively simple composition it catalyses the production of a rich variety of products from the non-thermal plasma conversion of CH_4 and CO_2 in nitrogen. The processes observed include the fixing of nitrogen to both HCN and acetamide, and the production of the chain oxides C_5O_2 and ketene. CO and formaldehyde are produced, in addition to unreacted but rotationally-excited CO_2 and CH_4, and a multicomponent liquid film. The Macor is essential to the formation of the liquid film, as is nitrogen gas, and the liquid film, in turn, plays an important role in the production of C_5O_2 and ketene. The formation of liquid products has been observed by others (see, for example, [16, 83]) but the possible wider significance of this has not hitherto been recognised: for example, by careful modification

of the liquid film with added solvent and/or by careful choice of model liquids, it could be possible to ensure that the plasma-induced chemistry takes place at and close to the plasma/liquid interface as modelling of the potential distribution using slabs of dielectrics shows that the discontinuity in the electric field will be highest at this interface. Hence we believe this approach may offer a new dimension to plasma catalytic chemistry, one that helps to transform the technology into a viable option for large scale chemical syntheses through a paradigm shift in plasma catalysis and reactor design.

Finally, it is clear that using Macor as a catalyst in the plasma-driven conversion of $CO_2 + CH_4 + N_2$ results in radically-different chemical processes to those observed in the analogous thermal experiments, supporting the contention that the two processes demand different, tailor-made catalysts identified using in-depth investigations of mechanism and kinetics.

Acknowledgements Abd Halim Bin Md Ali would like to thank the Government of Malaysia for a scholarship to study for a Ph.D., the staff of the Majlis Amanah Rakyat in Kuala Lumpur, Malaysia and London, United Kingdom for their invaluable assistance. Z. T. A. W. Mashhadani would like to thank the Government of Iraq for a Scholarship, the staff of the Higher Committee for Education Development in Iraq for their invaluable assistance and the Iraq Ministry of Oil Petroleum Research and Development Center PRDC for the opportunity to study for a Ph.D. The authors also wish to thank Mr. Neville Dickman and Mr. Simon Daley for their invaluable assistance and support for this work.

References

1. Whitehead JC (2016) Plasma–catalysis: the known knowns, the known unknowns and the unknown unknowns. J Phys D Appl Phys 49(24):243001
2. Aerts R, Martens T, Bogaerts A (2012) Influence of vibrational states on CO_2 splitting by dielectric barrier discharges. J Phys Chem C 116(44):23257–23273. https://doi.org/10.1021/jp307525t
3. Fridman A (2008) Plasma chemistry. Cambridge University Press, Cambridge. https://doi.org/10.1017/cbo9780511546075
4. Fridman AA, Rusanov VD (1994) Theoretical basis of non-equilibrium near atmospheric pressure plasma chemistry. Pure Appl Chem. https://doi.org/10.1351/pac199466061267
5. Chen HL, Lee HM, Chen SH, Chang MB (2008) Review of packed-bed plasma reactor for ozone generation and air pollution control. Ind Eng Chem Res 47:2122–2130
6. Kogelschatz U (2003) Dielectric-barrier discharges: their history, discharge physics and industrial applications. Plasma Chem Plasma Process 23(1):1–45
7. Malik MA, Hughes D, Heller R, Schoenbach KH (2015) Surface plasmas versus volume plasma: energy deposition and ozone generation in air and oxygen. Plasma Chem Plasma Process 35(4):697–704. https://doi.org/10.1007/s11090-015-9611-3
8. Zhang K, Mukhriza T, Liu X, Greco PP, Chiremba E (2015) A study on CO_2 and CH_4 conversion to synthesis gas and higher hydrocarbons by the combination of catalyst and dielectric-barrier discharges. Applied Catalysis A: General 502:138–149
9. Langleron M, Cavadias S, Amouroux J (1995) Study by mass spectrometry and gas chromatography of toluene oxidation in a low-pressure plasma reactor. Rapid Commun Mass Spectrom 9:18–22. https://doi.org/10.1002/rcm.1290090106
10. Nguyen VN, Blum L (2015) Syngas and synfuels from H_2O and CO_2: current status. Chem Ing Tec 87(4):354–375. https://doi.org/10.1002/cite.201400090
11. Xiao G, Xu W, Wu R, Ni M, Du C, Gao X, Luo Z, Cen K (2014) Non-thermal plasmas for VOCs abatement. Plasma Chem Plasma Process 34(5):1033–1065. https://doi.org/10.1007/s11090-014-9562-0

12. Scholtz V, Pazlarova J, Souskova H, Khun J, Julak J (2015) Nonthermal plasma—a tool for decontamination and disinfection. Biotechnol Adv 33(6, Part 2):1108–1119. https://doi.org/10.1016/j.biotechadv.2015.01.002
13. Ban L, Liu P, Ma C, Dai B (2013) Deep desulfurization of diesel fuels with plasma/air as oxidizing medium, diperiodatocuprate (III) as catalyzer and ionic liquid as extraction solvent. Plasma Sci Technol 15(12):1226–1231. https://doi.org/10.1088/1009-0630/15/12/12
14. Bai M, Leng B, Mao S, Li C (2016) Flue gas desulfurization by dielectric barrier discharge. Plasma Chem Plasma Process 36(2):511–521. https://doi.org/10.1007/s11090-015-9679-9
15. Zeng Y, Zhu X, Mei D, Ashford B, Tu X (2015) Plasma-catalytic dry reforming of methane over γ-Al_2O_3 supported metal catalysts. Catal Today 256(Part 1):80–87. https://doi.org/10.1016/j.cattod.2015.02.007
16. De Bie C, van Dijk J, Bogaerts A (2015) The dominant pathways for the conversion of methane into oxygenates and syngas in an atmospheric pressure dielectric barrier discharge. J Phys Chem C 119(39):22331–22350. https://doi.org/10.1021/acs.jpcc.5b06515
17. Ashford B, Tu X (2017) Non-thermal plasma technology for the conversion of CO_2. Curr Opin Green Sustain Chem 3(Supplement C):45–49. https://doi.org/10.1016/j.cogsc.2016.12.001
18. www.cpbg.com; www.defuma.com; www.babcock.com
19. www.ozonia.com; www.lenntech.com; www.evoqua.com
20. www.enerconind.com; www.alternor.com; www.plasmaetch.com; www.acxys.com
21. http://www.nap.edu/catalog/11960/plasma-science-advancing-knowledge-in-the-national-interest p 29–32
22. Jeong JY, Park J, Henins I, Babayan SE, Tu VJ, Selwyn GS, Ding G, Hicks RF (2000) Reaction chemistry in the afterglow of an oxygen − helium, atmospheric-pressure plasma. J Phys Chem A 104(34):8027–8032. https://doi.org/10.1021/jp0012449
23. Martin PA, Guelachvili G (1990) Velocity-modulation Fourier-transform spectroscopy of molecular ions. Phys Rev Lett 65(20):2535–2538
24. Benidar A, Guelachvili G, Martin PA (1991) Selective detection of OH radical in emission by concentration-modulation infrared FTS. Chem Phys Lett 177(6):563–567. https://doi.org/10.1016/0009-2614(91)90085-N
25. Shiqiang Z, van Wouter G, van Bram G, Sven H, van Eddie V, Annemie B, Peter B (2013) Spatially resolved ozone densities and gas temperatures in a time modulated RF driven atmospheric pressure plasma jet: an analysis of the production and destruction mechanisms. J Phys D Appl Phys 46(20):205202
26. Tu X, Whitehead JC (2014) Plasma dry reforming of methane in an atmospheric pressure AC gliding arc discharge: co-generation of syngas and carbon nanomaterials. Int J Hydrogen Energy 39(18):9658–9669. https://doi.org/10.1016/j.ijhydene.2014.04.073
27. Christensen PA, Hamnet A (1994) Techniques and mechanisms in electrochemistry. Blackie Academic & Professional Glasgow
28. Christensen PA (2010) In-situ Fourier transform infra red spectroelectrochemistry as a probe of electrocatalysis. In: Yarwood J, Douthwaite R, Duckett SB (eds) Spectroscopic properties of inorganic and organometallic compounds: techniques, materials and applications, vol 41. Royal Society of Chemistry, London, pp 125–165
29. Schmidt-Bleker A, Winter J, Iseni S, Dünnbier M, Weltmann KD, Reuter S (2014) Reactive species output of a plasma jet with a shielding gas device—combination of FTIR absorption spectroscopy and gas phase modelling. J Phys D Appl Phys 47(14):145201
30. Al-Abduly A, Christensen PA (2015) An in situ and downstream study of non-thermal plasma chemistry in an air fed dielectric barrier discharge (DBD). Plasma Sources Sci Technol 24:065006
31. Li K, Gabriel O, Meichsner J (2004) Fourier transform infrared spectroscopy study of molecular structure formation in thin films during hexamethyldisiloxane decomposition in low pressure rf discharge. J Phys D Appl Phys 37(4):588
32. Rivallan M, Fourré E, Aiello S, Tatibouët J-M, Thibault-Starzyk F (2012) Insights into the mechanisms of isopropanol conversion on γ-Al_2O_3 by dielectric barrier discharge. Plasma Process Polym 9(9):850–854. https://doi.org/10.1002/ppap.201200021
33. Stere CE, Adress W, Burch R, Chansai S, Goguet A, Graham WG, Hardacre C (2015) Probing a non-thermal plasma activated heterogeneously catalyzed reaction using in situ DRIFTS-MS. ACS Catal 5(2):956–964. https://doi.org/10.1021/cs5019265
34. Rodrigues A, Tatibouët J-M, Fourré E (2016) Operando DRIFT spectroscopy characterization of intermediate species on catalysts surface in VOC removal from air by non-thermal plasma assisted catalysis. Plasma Chem Plasma Process 36(4):901–915. https://doi.org/10.1007/s11090-016-9718-1
35. Jia Z, Rousseau A (2016) Sorbent track: quantitative monitoring of adsorbed VOCs under in situ plasma exposure. 6:31888. https://doi.org/10.1038/srep31888

36. Rivallan M, Aiello S, Thibault-Starzyk F (2010) Microsecond time-resolved Fourier transform infrared analytics in a low pressure glow discharge reactor. Rev Sci Instrum 81(10):103111. https://doi.org/10.1063/1.3492094
37. Christensen PA, Ali AHBM, Mashhadani ZTAW, Martin PA (2018) A direct Fourier transform infrared spectroscopic comparison of the plasma- and thermally-driven reaction of CO_2 at Macor. Plasma Chem Plasma Process 38(2):293–310. https://doi.org/10.1007/s11090-018-9874-6
38. Bevy LP (2006) Trends in catalysis research. Nova Science Publishers, Hauppauge
39. Christensen PA, Attidekou PS, Egdell RG, Maneelok S, Manning DAC (2016) An in situ FTIR spectroscopic and thermogravimetric analysis study of the dehydration and dihydroxylation of SnO_2: the contribution of the (100), (110) and (111) facets. Phys Chem Chem Phys 18(33):22990–22998
40. Aerts R, Somers W, Bogaerts A (2015) Carbon dioxide splitting in a dielectric barrier discharge plasma: a combined experimental and computational study. ChemSusChem 8(4):702–716
41. Herzberg G (1945) Molecular spectra and molecular structure. Vol. 2: Infrared and Raman spectra of polyatomic molecules. Van Nostrand Reinhold, New York
42. Stein SE "Infrared Spectra" in NST Chemistry Webbook, NIST Standard Reference Databace Number 69. National Institute od Standards and Technology. http://webbook.nist.gov/cgi/cbook.cgi?Contrib=MSDC-IR. Accessed September 5 2017
43. Bennett CJ, Jamieson CS, Kaiser RI (2010) Mechanistical studies on the formation and destruction of carbon monoxide (CO), carbon dioxide (CO_2), and carbon trioxide (CO_3) in interstellar ice analog samples. Phys Chem Chem Phys 12(16):4032–4050. https://doi.org/10.1039/B917162B
44. Al-Abduly AJ (2016) Fundamental and applied studies of non-thermal plasma. PhD thesis, Newcastle University
45. Frederick H, Van Zandt W (1947) The Infra-red spectrum of ketene. J Chem Phys 15(8):552–559. https://doi.org/10.1063/1.1746591
46. Ni C-K, Wade EA, Ashikhmin MV, Moore CB (1996) Infrared spectroscopy of ketene by two-step photodissociation. J Mol Spectrosc 177(2):285–293. https://doi.org/10.1006/jmsp.1996.0142
47. Corey SJ, Alexander MM, Ralf IK (2006) Understanding the kinetics and dynamics of radiation-induced reaction pathways in carbon monoxide ice at 10 K. Astrophys J Suppl Ser 163(1):184
48. Alexandre T, Robert LB (2004) Carbon-chain oxides in proton-irradiated CO ice films. Astrophys J 612(2):1214
49. Sicilia D, Ioppolo S, Vindigni T, Baratta GA, Palumbo ME (2012) Nitrogen oxides and carbon chain oxides formed after ion irradiation of CO:N_2 ice mixtures. Astron Astrophys 543:A155
50. British Chemical Abstracts (1937) Section A: general physical and inorganic chemistry, 575
51. Taeschler C (2000) Ketenes, ketene dimers, and related substances. In: Kirk–Othmer encyclopedia of chemical technology. Wiley Inc. https://doi.org/10.1002/0471238961.1105200501020105.a01.pub2
52. Ketene Market - Global Industry Analysis, Size, Share, Growth, Trends and Forecast 2014–2020 (2017). Transparency market research Albany NY, United States
53. Allen AD, Tidwell TT (2013) Ketenes and other cumulenes as reactive intermediates. Chem Rev 113(9):7287–7342. https://doi.org/10.1021/cr3005263
54. Boganov SE, Kudryashov SV, Ryabov AY, Suslov AI, Rynin SS, Egorov MP, Nefedov OM (2014) Matrix IR study of benzene transformations in a pulsed glow discharge in the absence and the presence of oxygen. Plasma Chem Plasma Process 34(6):1345–1370. https://doi.org/10.1007/s11090-014-9576-7
55. Marko F, Pavlo M, Alexander MM, Ralf IK (2016) Pentacarbon dioxide (C_5O_2) formation and its role as a tracer of solar system evolution. Astrophys J Lett 818(2):L30
56. Vastel C, Ceccarelli C, Lefloch B, Bachiller R (2014) The origin of complex organic molecules in prestellar cores. Astrophys J Lett 795(1):L2
57. Choi KN, Barker EF (1932) Infrared absorption spectrum of hydrogen cyanide. Phys Rev 42(6):777–785
58. Herzberg G (2008) Molecular spectra and molecular structure. Vol 1: infrared and Raman spectra of diatomic molecules, 2nd edn. Van Nostrand Reinhold, New York
59. Bolis V, Fubini B, Garrone E, Morterra C (1989) Thermodynamic and vibrational characterization of CO adsorption on variously pretreated anatase. J Chem Soc, Faraday Trans 1 Phys Chem Condens Phases 85(6):1383–1395. https://doi.org/10.1039/F19898501383
60. Martini LM, Dilecce G, Guella G, Maranzana A, Tonachini G, Tosi P (2014) Oxidation of CH_4 by CO_2 in a dielectric barrier discharge. Chem Phys Lett 593(Supplement C):55–60. https://doi.org/10.1016/j.cplett.2013.12.069
61. Henry HBJ (1955) The infrared absorption spectrum of formaldehyde vapor. Ph.D Thesis, Ohio State University
62. Gratien A, Picquet-Varrault B, Orphal J, Perraudin E, Doussin JF, Flaud JM (2007) Laboratory intercomparison of the formaldehyde absorption cross sections in the infrared (1660–1820 cm^{-1}) and

ultraviolet (300–360 nm) spectral regions. J Geophys Res Atmos. https://doi.org/10.1029/2006JD007201
63. Xu S, Whitehead JC, Martin PA (2017) CO_2 conversion in a non-thermal, barium titanate packed bed plasma reactor: The effect of dilution by Ar and N_2. Chem Eng J 327(Supplement C):764–773. https://doi.org/10.1016/j.cej.2017.06.090
64. Ramakers M, Michielsen I, Aerts R, Meynen V, Bogaerts A (2015) Effect of argon or helium on the CO_2 conversion in a dielectric barrier discharge. Plasma Process Polym 12(8):755–763. https://doi.org/10.1002/ppap.201400213
65. Snoeckx R, Heijkers S, Van Wesenbeeck K, Lenaerts S, Bogaerts A (2016) CO_2 conversion in a dielectric barrier discharge plasma: N_2 in the mix as a helping hand or problematic impurity? Energy Environ Sci 9(3):999–1011. https://doi.org/10.1039/C5EE03304G
66. Danko M, Orszagh J, Ďurian M, Kočišek J, Daxner M, Zöttl S, Maljković JB, Fedor J, Scheier P, Denifl S, Matejčík S (2013) Electron impact excitation of methane: determination of appearance energies for dissociation products. J Phys B At Mol Opt Phys 46(4):045203
67. Stano M, Matejcik S, Skalny JD, Märk TD (2003) Electron impact ionization of CH_4: ionization energies and temperature effects. J Phys B: At Mol Opt Phys 36(2):261
68. Velchev I, Hogervorst W, Ubachs W (1999) Precision VUV spectroscopy of Ar I at 105 nm. J Phys B At Mol Opt Phys 32(17):L511
69. Hagelaar GJM, Pitchford LC (2005) Solving the Boltzmann equation to obtain electron transport coefficients and rate coefficients for fluid models. Plasma Sources Sci Technol 14(4):722
70. Quirico E, Montagnac G, Lees V, McMillan PF, Szopa C, Cernogora G, Rouzaud J-N, Simon P, Bernard J-M, Coll P, Fray N, Minard RD, Raulin F, Reynard B, Schmitt B (2008) New experimental constraints on the composition and structure of tholins. Icarus 198(1):218–231. https://doi.org/10.1016/j.icarus.2008.07.012
71. Imanaka H, Khare BN, Elsila JE, Bakes ELO, McKay CP, Cruikshank DP, Sugita S, Matsui T, Zare RN (2004) Laboratory experiments of Titan tholin formed in cold plasma at various pressures: implications for nitrogen-containing polycyclic aromatic compounds in Titan haze. Icarus 168(2):344–366. https://doi.org/10.1016/j.icarus.2003.12.014
72. Horvath G, Mason N, Polachova L, Zahoran M, Moravský L, Matejcik S (2010) Packed bed DBD discharge experiments in admixtures of N_2 and CH_4. Plasma Chem Plasma P 30(5):565–577. https://doi.org/10.1007/s11090-010-9241-8
73. Snoeckx R, Setareh M, Aerts R, Simon P, Maghari A, Bogaerts A (2013) Influence of N2 concentration in a CH4/N2 dielectric barrier discharge used for CH4 conversion into H2. Int J Hydrogen Energy 38(36):16098–16120. https://doi.org/10.1016/j.ijhydene.2013.09.136
74. Frost DC, McDowell CA (1956) The Dissociation Energy of the Nitrogen Molecule. Proc R Soc Lond A 236(1205):278–284
75. Roeges NPG (1994) A Guide to the Complete Interpretation of Infrared Spectral of Organic Structures. Wiley
76. Socrates G (1980) Infrared and Raman Characteristic Group Frequencies: Tables and Charts. John Wiley and Sons, Chichester
77. Hollis JM, Lovas FJ, Anthony JR, Jewell PR, Ilyushin VV, Kleiner I (2006) Detection of Acetamide (CH3CONH2): the Largest Interstellar Molecule with a Peptide Bond. The Astrophysical Journal Letters 643(1):L25
78. Rumbach P, Bartels DM, Sankaran RM, Go DB (2015) The solvation of electrons by an atmospheric-pressure plasma. Nature Communications 6:7248. https://doi.org/10.1038/ncomms8248. https://www.nature.com/articles/ncomms8248#supplementary-information
79. Maeda Y, Iizuka Y, Kohyama M (2013) Generation of Oxygen Vacancies at a Au/TiO2 Perimeter Interface during CO Oxidation Detected by in Situ Electrical Conductance Measurement. J Am Chem Soc 135(2):906–909. https://doi.org/10.1021/ja310999c
80. Kim H-H, Teramoto Y, Negishi N, Ogata A (2015) A multidisciplinary approach to understand the interactions of nonthermal plasma and catalyst: A review. Catalysis Today 256 (Part 1):13-22. https://doi.org/10.1016/j.cattod.2015.04.009
81. Hyatt JA, Raynolds PW (2004) Ketene Cycloadditions. In: Organic Reactions. John Wiley & Sons, Inc. https://doi.org/10.1002/0471264180.or045.02
82. Scarduelli G, Guella G, Ascenzi D, Tosi P (2011) Synthesis of Liquid Organic Compounds from CH4 and CO2 in a Dielectric Barrier Discharge Operating at Atmospheric Pressure. Plasma Processes Polym 8(1):25–31. https://doi.org/10.1002/ppap.201000044
83. Havran V, Duduković MP, Lo CS (2011) Conversion of Methane and Carbon Dioxide to Higher Value Products. Ind Eng Chem Res 50(12):7089–7100. https://doi.org/10.1021/ie2000192